Biodistribution and Radiation Dosimetry of ^{18}F-CP-18, a Potential Apoptosis Imaging Agent, as Determined from PET/CT Scans in Healthy Volunteers

Mohan Doss[1], Hartmuth C. Kolb[2], Joseph C. Walsh[2], Vani Mocharla[2], Hong Fan[3], Ashok Chaudhary[3], Zhihong Zhu[3], R. Katherine Alpaugh[4], Miriam N. Lango[5], and Jian Q. Yu[1]

[1]Diagnostic Imaging, Fox Chase Cancer Center, Philadelphia, Pennsylvania; [2]Siemens Molecular Imaging Inc., Culver City, California; [3]Siemens Molecular Imaging Inc., North Wales, Pennsylvania; [4]Protocol Support Lab, Fox Chase Cancer Center, Philadelphia, Pennsylvania; and [5]Department of Surgical Oncology, Fox Chase Cancer Center, Philadelphia, Pennsylvania

^{18}F-CP-18, or (18S,21S,24S,27S,30S)-27-(2-carboxyethyl)-21-(carboxymethyl)-30-((2S,3R,4R,5R,6S)-6-((2-(4-(3-F18-fluoropropyl)-1H-1,2,3-triazol-1-yl)acetamido)methyl)-3,4,5-trihydroxytetrahydro-2H-pyran-2-carboxamido)-24-isopropyl-18-methyl-17,20,23,26,29-pentaoxo-4,7,10,13-tetraoxa-16,19,22,25,28-pentaazadotriacontane-1,32-dioic acid, is being evaluated as a tissue apoptosis marker for PET imaging. The purpose of this study was to determine the biodistribution and estimate the normal-organ radiation-absorbed doses and effective dose from ^{18}F-CP-18. **Methods:** Successive whole-body PET/CT scans were obtained at approximately 7, 45, 90, 130, and 170 min after intravenous injection of ^{18}F-CP-18 in 7 healthy human volunteers. Blood samples and urine were collected between the PET/CT scans, and the biostability of ^{18}F-CP-18 was assessed using high-performance liquid chromatography. The PET scans were analyzed to determine the radiotracer uptake in different organs. OLINDA/EXM software was used to calculate human radiation doses based on the biodistribution of the tracer. **Results:** ^{18}F-CP-18 was 54% intact in human blood at 135 min after injection. The tracer cleared rapidly from the blood pool with a half-life of approximately 30 min. Relatively high ^{18}F-CP-18 uptake was observed in the kidneys and bladder, with diffuse uptake in the liver and heart. The mean standardized uptake values (SUVs) in the bladder, kidneys, heart, and liver at around 50 min after injection were approximately 65, 6, 1.5, and 1.5, respectively. The calculated effective dose was 38 $\pm$ 4 μSv/MBq, with the urinary bladder wall having the highest absorbed dose at 536 $\pm$ 61 μGy/MBq using a 4.8-h bladder-voiding interval for the male phantom. For a 1-h voiding interval, these doses were reduced to 15 $\pm$ 2 μSv/MBq and 142 $\pm$ 15 μGy/MBq, respectively. For a typical injected activity of 555 MBq, the effective dose would be 21.1 $\pm$ 2.2 mSv for the 4.8-h interval, reduced to 8.3 $\pm$ 1.1 mSv for the 1-h interval. **Conclusion:** ^{18}F-CP-18 cleared rapidly through the renal system. The urinary bladder wall received the highest radiation dose and was deemed the critical organ. Both the effective dose and the bladder dose can be reduced by frequent voiding. From the radiation dosimetry perspective, the apoptosis imaging agent ^{18}F-CP-18 is suitable for human use.

Key Words: ^{18}F-CP-18; biodistribution; internal dosimetry; apoptosis marker; PET

J Nucl Med 2013; 54:2087–2092
DOI: 10.2967/jnumed.113.119800

Programmed cell death, known as apoptosis, is a regulated cellular mechanism that maintains cell population homeostasis and prevents the proliferation of unwanted or damaged cells (*1*). When apoptosis becomes unregulated, biologic dysfunction ensues and is a contributing factor in the onset of autoimmune diseases, ischemic heart failure, and even transplant rejection. A cell's apoptotic potential can also be reduced or even halted, a common trait of cancer cells as they progress into malignant phenotypes (*2,3*).

The apoptotic process invokes distinct biochemical alterations triggered by either extrinsic signaling via the death receptor or through intrinsic pathways via mitochondrial signaling. Regardless of how apoptosis is initiated, the signaling pathways ultimately converge at the execution phase, which commits the cell to undergo apoptosis and eventually die. Interestingly, apoptosis directed via the mitochondria initiates the release of proapoptotic proteins, which activates a family of cysteinyl aspartate proteases (caspases) as critical mediators of the intrinsic apoptosis pathway. Although caspase proteins are involved in the initiation of apoptosis (caspase-2, -8, -9, and -10), the executioners (caspase-3, -6, and -7) cleave multiple intracellular substrates to provoke the apoptotic cascade. Caspase-3, as a downstream apoptosis effector, cleaves key proteins involved in DNA repair (PARP [poly ADP ribose polymerase; ADP = adenosine diphosphate]), signaling proteins (Akt [protein kinase B], Ras [rat sarcoma]), and cell cycle regulators (p27Kip1). The detection of activated caspase-3 could therefore be a valuable and specific tool for identifying apoptotic cells before the morphologic tissue changes.

Several ^{18}F-labeled PET imaging agents have been developed for the in vivo detection of apoptosis. The PET-labeled agents ^{18}F-ML10 (*4–6*), ^{18}F-C2A (*7*), ^{18}F-annexin-V (*8–10*), and ^{18}F-FBnTP (*11,12*) detect key apoptotic pathways involved in membrane imprints (*13*), membrane blebbing, or mitochondrial membrane potential but do not specifically target members of the caspase family. A separate class of PET imaging agents based on the small-molecule isatin scaffold has been developed including ^{18}F-AF-110 (*14*), ^{18}F-ICMT-11 (*15,16*), ^{11}C-WC-98, ^{18}F-WC-II-89,

Received Jan. 15, 2013; revision accepted Jun. 17, 2013.
For correspondence or reprints contact: Jian Q. Yu, Diagnostic Imaging, Fox Chase Cancer Center, 333 Cottman Ave., Philadelphia, PA 19111.
E-mail: Michael.Yu@fccc.edu
Published online Oct. 17, 2013.
COPYRIGHT © 2013 by the Society of Nuclear Medicine and Molecular Imaging, Inc.

and ^{18}F-WC-IV-3 (*14,17–19*). The utility of these ^{18}F-radiolabeled isatins as PET apoptosis imaging agents has been described previously (*15,16,19–21*). Several isatin-based radiotracers are reported to undergo hepatic-based metabolism and gut clearance, which may limit abdominal imaging applications (*15,16*). In addition, radiolabeled isatins can potentially bind other cysteine proteases (e.g., cathepsins), which may lower the specificity of these tracers in imaging apoptosis (*22*).

^{18}F-CP-18 was designed as a caspase-3 peptide substrate, similar in principle to fluorescent reporters that are used in caspase-3 activity assays. ^{18}F-CP-18 bears the tetra-peptidic caspase-3 recognition sequence (D-E-V-D), which has high specificity for caspase-3 (*23*), and a polyethylene glycol (PEG) chain to facilitate membrane transport into cells, which is necessary because the high polar DEVD peptide sequence itself poorly diffuses across cell membranes. Even though ^{18}F-CP-18 contains multiple peptide functional groups, the tracer is readily radiolabeled with ^{18}F using click-chemistry, a technique that couples primary azides and terminal alkynes in the presence of Cu(I) to selectively form 1,2,3-triazoles (*24–26*). From a mechanistic standpoint, the cell-permeating PEG moiety facilitates the internalization of ^{18}F-CP-18 into cells undergoing cleavage in the presence of active intracellular caspase-3. This cleavage step effectively traps the polar radiolabeled fragment within the cell as a function of caspase-3 activity. As more ^{18}F-CP-18 is cleaved inside the dying cell, more labeled fragments are accumulated, resulting in signal enhancement. The localization of ^{18}F-CP-18 in apoptotic tissues has been previously evaluated in preclinical models (*27*). Further exploration of its use as an apoptosis marker in patients is warranted.

The main goal of this study was to determine the biodistribution and dosimetry of ^{18}F-CP-18 in humans using PET.

MATERIALS AND METHODS

Radiopharmaceutical Preparation

The name of the investigational product being studied in this protocol is ^{18}F-CP-18, or (18S,21S,24S,27S,30S)-27-(2-carboxyethyl)-21-(carboxymethyl)-30-((2S,3R,4R,5R,6S)-6-((2-(4-(3-F18-fluoropropyl)-1H-1,2,3-triazol-1-yl)acetamido)methyl)-3,4,5-trihydroxytetrahydro-2H-pyran-2-carboxamido)-24-isopropyl-18-methyl-17,20,23,26,29-pentaoxo-4,7,10,13-tetraoxa-16,19,22,25,28-pentaazadotriacontane-1,32-dioic acid. The chemical structure of ^{18}F-CP-18 is shown in Figure 1.

^{18}F labeling was performed in an automated synthesis module having minor hardware reconfigurations. A solution of anhydrous ^{18}F-fluoride complexed with 4,7,13,16,21-pentaoxa-1,10-diazabicyclo [8.8.5]tricosane (Sigma Aldrich) and potassium carbonate in acetonitrile was reacted with pent-4-yn-1-yl 4-methylbenzenesulfonate to generate ^{18}F-fluoropentyne. This ^{18}F-labeled intermediate was then reacted with the CP-18 azide precursor, sodium ascorbate, $CuSO_4$, and tris[(1-benzyl-1H-1,2,3-triazol-4-yl)methyl]amine (TBTA) dissolved in a solution of ethanol:water:acetonitrile (Fig. 2). The crude reaction mixture was purified via semipreparative high-performance liquid chromatography (HPLC) and reformulated using a C18 SepPak (Waters) cartridge to achieve a final formulation of ^{18}F-CP-18 in a maximum of 10% ethanol:water (v/v). The solution was then processed through a 0.22-μm sterile filter into a sterile vial. The average decay-corrected radiochemical yield of ^{18}F-CP-18 was 18.7%, and the average specific activity was 171,093 MBq/μmol (n = 7).

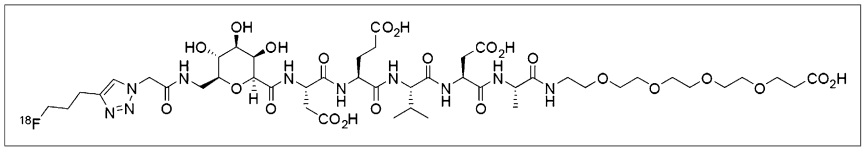

FIGURE 1. Chemical structure of ^{18}F-CP-18.

Subjects

The study was approved by the Research Review Committee, Institutional Review Board, and Radiation Safety Committee of Fox Chase Cancer Center. Seven healthy volunteers (5 women, 2 men; mean age ± SD, 50 ± 9 y; age range, 31–55 y) were included in the study. Written informed consent was obtained from each subject. The subjects' weights were 71 ± 8 kg (range, 59–82 kg). All subjects were healthy based on medical history, physical examination, electrocardiogram, urinalysis, and standard blood tests.

PET/CT Acquisition and Image Analysis

After the intravenous injection of 604 ± 74 MBq (range, 537–699 MBq) of ^{18}F-CP-18 to the volunteers, 5 successive whole-body PET/CT scans were obtained on a Biograph Truepoint 16 PET/CT scanner (Siemens Healthcare). A low milliampere setting on the scanner was used to obtain the CT scans for attenuation correction and organ localization. The helical CT scan acquisition parameters were 130 kVp, 20 mA, a 0.6-s rotation, and a pitch of 1.

The whole-body PET scans were acquired in 3-dimensional mode and ranged from the top of the head down to mid thigh. The 5 whole-body scans were conducted at approximately 7, 45, 90, 130, and 170 min after injection. The scan time was 1.5 min per bed position, and each scan covered 8 or 9 bed positions. In addition, after the first whole-body scan, a PET/CT scan of the mid thigh to toes was obtained. Blood pressure, body temperature, respiratory rate, pulse, and electrocardiogram were monitored before the administration of ^{18}F-CP-18; after the first, second, and last PET/CT scans; and then at 24 h after the dose administration.

Blood and urine were collected before the radiotracer injection and in the breaks between the PET scans. Urine was also collected at the end of the last PET scan. Samples of urine were assayed in a well counter to estimate the excreted activity in urine. HPLC was performed to determine the amounts of intact ^{18}F-CP-18 and its radioactive metabolites in the plasma. Briefly, the activity of the whole-blood samples was measured in a well counter as counts per minute. Of the 7 blood samples submitted for analysis, 1 was not analyzed because of technical difficulties with the HPLC instrumentation. For the remaining 6 blood samples, the whole blood was centrifuged at 3,500 RPM for 5 min to separate plasma from whole cells. The plasma fraction was removed and placed in a separate, empty, preweighed tube to record the weight of plasma. An aliquot of plasma (400 μL) was removed, followed by spiking of the aliquot with a nonradioactive CP-18 standard (16 μL of a 1 mg/mL aqueous stock solution) and acetonitrile (100 μL). After the sample was stirred for 30 s and centrifuged at 13,000 RPM for 8 min to separate proteins from plasma, the plasma supernatant was removed and weighed, and the counts per minute of pellet and extract were measured. An aliquot (50–100 μL) of the processed plasma sample was injected into the HPLC loop (1100 HPLC system [Agilent] equipped with a Luna C18 analytic column [10 μm, 250 × 4.5 mm; Phenomenex]; mobile phases, A: water w/0.05% trifluoroacetic acid (TFA) and B: acetonitrile w/0.05% TFA; gradient 95% A to 50% A in 15 min; ultraviolet absorbance 200 or 206 nm; flow rate, 1 mL/min). The radio-HPLC eluent was collected in 1-min fractions and individually counted, and the percentage of plasma-borne activity in the form of parent compound (i.e., ^{18}F-CP-18) and in the form of metabolites was extracted from the radio-HPLC traces.

The PET scans were reconstructed to a 62-cm display field of view using the Siemens

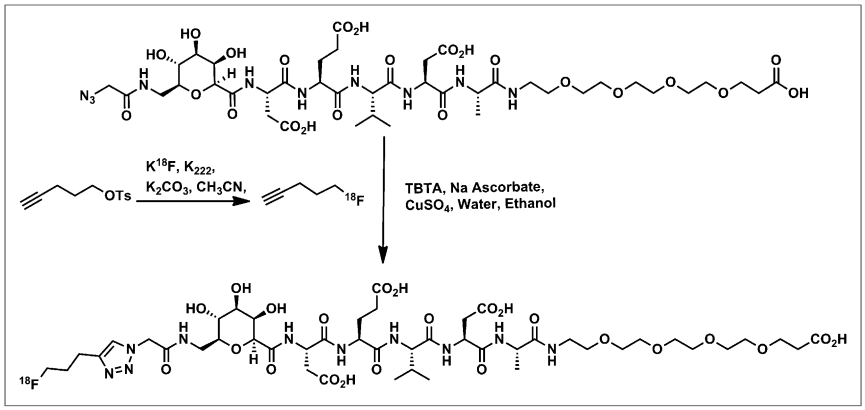

FIGURE 2. Synthesis of ^{18}F-CP-18 from precursor.

TrueX reconstruction algorithm with 21 subsets and 2 iterations and a gaussian postprocessing filter of 4 mm in full width at half maximum. The reconstruction included corrections for random coincidences and scatter. Attenuation correction was applied using the low-dose CT. The accuracy of the activity in the PET images was verified by summing the activity in the first whole-body PET scan and the PET scan from mid thigh to toes and comparing the total-body activity thus calculated with the decayed injected activity.

The PET images for the middle time point for each patient were displayed on an imaging workstation. For each of the following organs including brain, liver, heart, spleen, kidneys, bladder, breasts (for females), and testes (for males), volume regions of interest (ROIs) were drawn. The PET images for other time points were displayed and registered with this PET scan to transfer the respective volume ROIs and determine the total activity in each organ. Adjustments to the individual ROIs were made to ensure the inclusion of the respective organs. The percentage of the injected activity in each organ was determined at each imaging time point.

Normalized Number of Disintegrations

The percentage administered activity for each organ for each time point was fitted to an exponential or sum of exponentials function in OLINDA/EXM software (*28*) to determine the total number of disintegrations per unit administered activity, hereafter referred to as the normalized number of disintegrations. Activity in the remainder of the body was calculated for each time point as the injected activity minus the activity in all the source organs and in collected urine. The half-times for biologic excretion were computed by exponential fitting of injected activity minus accumulated urine activity as a function of time. The 1.0- and 4.8-h bladder-voiding intervals in OLINDA/EXM were used to determine the normalized number of disintegrations in the bladder. Absorbed doses to the various organs were calculated by entering the normalized number of disintegrations of all source organs for each subject into OLINDA/EXM, using the standard adult male and female models.

RESULTS

The injection of ^{18}F-CP-18 (604 ± 74 MBq) in the 7 subjects produced no clinically significant effects on either the vital signs (blood pressure, temperature, respiratory rate, pulse, and electrocardiogram) or the blood tests during the 3-h observation period after administration and in the follow-up visit at 24 h.

The analysis of plasma samples of 6 healthy human subjects showed that the ^{18}F-CP-18 metabolized slowly with the percentage of plasma-borne activity in the form of ^{18}F-CP-18 decreasing from 99% to 52% from 5 to 135 min after injection. On the basis of these plasma activity measurements, ^{18}F-CP-18–derived activity exhibited a clearance half-time of approximately 30 min. The radio-HPLC trace indicated that one metabolite was present in plasma along with the parent compound (Supplemental Fig. 1; supplemental materials are available at http://jnm.snmjournals.org). On the basis of the relative retention time of the metabolite peak, the plasma metabolite is tentatively assigned as the fragment cleaved between DE and VD. This pattern of cleavage is consistent with metabolites observed in mice for which those metabolites were identified by mass spectroscopy (data not shown). Urine analysis revealed the presence of the parent tracer ranging from 37% at 35 min to 21% at 135 min (Supplemental Fig. 1). The urine samples contained predominantly 2 major metabolites in combined percentages of 63% and 79% after 35 and 135 min, respectively. The enrichment of metabolites in the urine relative to the parent compound suggests a faster clearance rate for the metabolites relative to the intact tracer. Again, on the basis of relative retention time analysis of the metabolite signals, these fragments are tentatively assigned as the DE fragment and the parent tracer minus the PEG group, respectively.

Figure 3 displays PET maximum-intensity-projection images for one of the subjects from the PET scans. In the first scan, the predominant uptake was seen in both the kidneys and the urinary bladder, with moderate uptake observed in the liver, heart, and testes. All other organs had near-background levels of activity. The mean SUVs at about 50 min after injection were approximately 65 in the bladder, 6 in the kidneys, and 1.5 in both the heart and the liver. The rest of the body had much lower SUVs. The time–activity data for the urinary bladder, liver, and kidneys are shown in Figure 4. There was large intersubject variation in both the bladder uptake (16%–27%) and the kidney uptake (3.5%–11%), as indicated by the large error bars. The renal system (kidneys and bladder together) had more consistent uptake, ranging from 22% to 31%. The liver had the

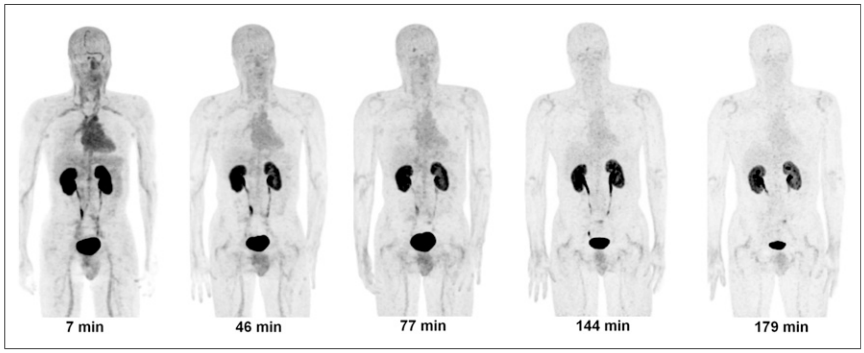

FIGURE 3. Decay-corrected anterior maximum-intensity projections of PET at 7, 46, 77, 144, and 179 min (from left to right) after injection of ^{18}F- CP-18 in male volunteer. There was rapid clearance of activity in all organs.

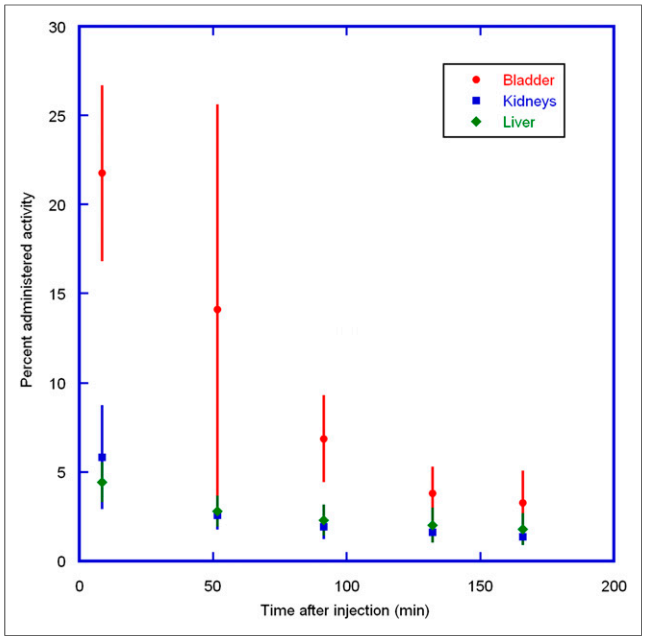

FIGURE 4. Mean percentage administered activity and SD for bladder, kidneys, and liver determined on basis of seven ^{18}F-CP-18 PET emission scans in human volunteers, as function of time after injection. Rapid clearance of activity was observed in organs.

next highest uptake, ranging from 3.2% to 5.7%. The study radiotracer was excreted primarily via the renal system. By the end of the study (~2.8 h), approximately 77% of the injected activity of ^{18}F-CP-18 had been excreted in the urine, as determined by assaying the urine samples in a well counter.

The normalized number of disintegrations for the organs is listed in Table 1. The mean organ doses are given in Table 2. The mean (±SD) effective dose of ^{18}F-CP-18 for the human adult male phantom was 15 ± 2 and 38 ± 4 μSv/MBq for the 1- and 4.8-h bladder-voiding interval, respectively. For a typical injected dose of ^{18}F-CP-18 (555 MBq), the effective doses for the 2 intervals were 8.3 ± 1.1 and 21.1 ± 2.2 mSv, respectively. The adult female phantom doses were 20%–34% higher. The 2 organs with the highest radiation-absorbed doses were the urinary bladder wall and kidneys. For the 4.8-h bladder-voiding interval, the dose to uterus was similar to the dose to the kidneys.

DISCUSSION

^{18}F-CP-18, which is currently under evaluation for detecting tumor apoptosis (*27*), was investigated in this dosimetry study in healthy volunteers. In this investigation, ^{18}F-CP-18 was shown to have reasonable biodistribution and dosimetry profiles in human subjects, suggesting this agent may have promise in PET imaging. This study provides information on the background uptake levels in normal organs. The data also address the potential radiation exposure in humans through whole-body PET imaging.

^{18}F-CP-18 displayed a biodistribution profile dominated by activity uptake in both the bladder and the kidneys indicative of a rapid renal clearance. Accordingly, 77% of injected activity was excreted within 2.8 h after injection of the tracer. The liver and heart showed diffuse uptake, and there was no evidence of the tracer above background levels in the large intestines during the 2.8-h imaging period, consistent with the notion that the tracer is cleared predominantly via the renal system. The rapid clearance and relatively low nonspecific uptake of the tracer, as compared with other ^{18}F-labeled apoptosis imaging agents, suggest that a large imaging window is possible for detecting increased caspase-3 expression in tumors throughout the torso, including the lungs, breast, and head and neck regions.

Among all the organs observed, the urinary bladder wall received the highest dose with the 4.8-h bladder-voiding interval as a result of the tracer's clearance profile. The mean urinary bladder wall doses were 142 ± 15 and 536 ± 61 μGy/MBq for the 1- and 4.8-h bladder-voiding intervals, respectively. Kidneys had the next highest dose, 39 ± 10 μGy/MBq, followed by the uterus at 38 ± 3 μGy/MBq for the 4.8-h bladder-voiding interval. The testes had doses of 29 and 25 μGy/MBq for the 2 intervals, respectively. The remaining organs had lower doses, in the range of 2–20 μGy/MBq. The average values of effective dose for ^{18}F-CP-18 were 15 ± 2 and 38 ± 4 μSv/MBq, respectively, for the 2 intervals. For a typical 555-MBq injected dose of ^{18}F-CP-18, the effective dose for the 4.8-h interval is 21.1 ± 2.2 mSv. The effective dose is lower than the 30-mSv dose limit specified by the Food and Drug Administration for research subjects (*29*). By more frequent bladder voiding, the doses can be reduced. For the 1-h bladder-voiding interval, the effective dose was reduced to 8.3 ± 1.1 mSv.

^{18}F-CP-18 was found to be initially stable in human plasma and about 54% intact at 135 min after injection. The urine analysis suggests that the metabolites and parent tracer are predominantly excreted via the urine. The metabolites formed are tentatively assigned as the expected cleavage products of the parent D-E-V-D sequence, which were previously observed during the preclinical evaluation of the tracer in rodents (data not shown) (*27*). Most metabolite activity cleared quickly through urine via the kidneys though a small amount was detectable in plasma. The combination of the clearance and biostability profile suggests that this tracer is suitable for imaging tissue apoptosis in humans.

Table 3 compares the doses to individual organs for ^{18}F-CP-18 with ^{18}F-FDG for the bladder-voiding interval of 4.8 h (*30*). The absorbed doses in the brain, heart, pancreas, lungs, spleen, thymus, thyroid, and stomach wall were much lower for ^{18}F-CP-18 than those for ^{18}F-FDG. ^{18}F-CP-18 did not appreciably cross the blood–brain barrier in our imaging studies. The absorbed doses in urinary

TABLE 1
Normalized Number of Disintegrations of Source Organs for Volunteers Injected with ^{18}F-CP-18

Organ	Normalized no. of disintegrations (MBq-h/MBq administered)
Breasts	0.015 ± 0.0047
Brain	0.0089 ± 0.0038
Heart contents	0.026 ± 0.0036
Kidneys	0.059 ± 0.017
Liver	0.064 ± 0.024
Spleen	0.0090 ± 0.0024
Testes*	0.0057 ± 0.0017
Urinary bladder wall	
1.0 h	0.29 ± 0.033
4.8 h	1.1 ± 0.13
Remainder	0.82 ± 0.14

*Data from 2 male subjects only.
Data are mean ± SD; n = 7.

TABLE 2
Estimated Organ Doses per Unit Administered Activity for ^{18}F-CP-18 for Human Adult Male Phantom

Organ	4.8-h void interval (μGy/MBq)	1-h void interval (μGy/MBq)
Adrenals	6.8 ± 0.8	6.4 ± 0.8
Brain	2.4 ± 0.6	2.4 ± 0.6
Breasts	7.7 ± 3.6	7.7 ± 3.6
Gallbladder wall	7.6 ± 0.8	6.7 ± 0.9
Heart wall	10 ± 0.8	10 ± 0.8
Kidneys	39 ± 10	39 ± 10
Liver	11 ± 3.0	10 ± 3.0
Lower large intestine wall	20 ± 1.3	8.8 ± 0.5
Lungs	4.7 ± 0.7	4.6 ± 0.7
Muscle	8.1 ± 0.4	5.3 ± 0.6
Osteogenic cells	7.9 ± 0.9	6.8 ± 1.0
Ovaries	19 ± 1.1	8.7 ± 0.6
Pancreas	6.9 ± 0.8	6.5 ± 0.8
Red marrow	6.8 ± 0.4	4.9 ± 0.6
Skin	4.7 ± 0.4	3.7 ± 0.5
Small intestine	11 ± 0.5	6.8 ± 7
Spleen	13 ± 2.5	13 ± 2.6
Stomach wall	6.1 ± 0.7	5.5 ± 0.8
Testes*	25 ± 14	29 ± 6.7
Thymus	4.8 ± 0.7	4.8 ± 0.7
Thyroid	4.2 ± 0.7	4.2 ± 0.7
Upper large intestine wall	9.7 ± 0.5	6.4 ± 0.7
Urinary bladder wall	536 ± 61	142 ± 15
Uterus	38 ± 3.2	14 ± 0.6
Total body	8.2 ± 0.4	5.6 ± 0.6

*Data from 2 male subjects only.
Data are mean ± SD; $n = 7$. Effective doses (μSv/MBq) were 38 ± 3.9 for 4.8-h and 15 ± 1.9 for 1-h void interval.

bladder, kidneys, testes, and uterus were higher for ^{18}F-CP-18 than for ^{18}F-FDG. A large fraction of ^{18}F-CP-18 (~77% in 2.8 h) was excreted through the urinary system. The urinary bladder wall dose for ^{18}F-CP-18 (540 μGy/MBq) was much higher than that for ^{18}F-FDG (190 μGy/MBq) (with 4-h bladder-voiding interval). However, if patients void frequently, the bladder dose is reduced to approximately 142 μGy/MBq using a 1-h bladder-voiding interval.

A successful apoptosis imaging agent will localize within apoptotic tissue with sufficient contrast between apoptotic and nonapoptotic tissues. Within normal tissues, elevated levels of caspase-3 exist for tissue maintenance, especially within cartilage and in mammary glands (*31*). With these tissues used as internal controls, PET images in several subjects reveal elevated uptake of ^{18}F-CP-18 in both shoulder cartilage and mammary glands relative to non–caspase-expressing tissue (e.g., muscle), consistent with differences in caspase-3 expression levels observed across such tissues (*31*). As a second confirmation that ^{18}F-CP-18 is targeting tissue apoptosis, the SPECT apoptosis imaging agent ^{99m}Tc-EC annexin V also appeared to exhibit uptake in shoulder cartilage similar to ^{18}F-CP18, suggesting that both tracers target an overlapping pathology (*32*). The biodistribution and radiation dosimetry of ^{18}F-CP-18 are likely compatible with its use as a PET apoptosis imaging agent. Although the current imaging doses and scan times allowed for visualization of these caspase-expressing tissues, further imaging optimization studies will be required to determine the optimal scan time and dose levels for imaging apoptosis, or apoptotic fractions thereof, especially within tumors. From the data obtained in this study, PET imaging at 30 min after injection appears to be optimal, in comparison to the 60-min delay that is typically used for other ^{18}F-based imaging compounds such as ^{18}F-FDG.

As a potential therapy target, apoptosis presents a unique opportunity for enabling a personalized medicine approach. For example, apoptosis imaging has the potential to identify treatment-resistant tumors in need of alternate therapies by monitoring changes in ^{18}F-CP18 uptake during the course of therapy, especially in instances where metabolic ^{18}F-FDG PET imaging data are confounded by tissue inflammation. Given that all tumors undergo apoptosis to varying degrees, a change in apoptosis after treatment is likely to be more meaningful than a single baseline apoptosis scan. Serial tumor uptake measurements are relatively easily performed using noninvasive PET imaging as a semiquantitative tool, which is a distinct advantage over the use of multiple biopsies.

PET apoptosis imaging may also enable the development of novel apoptosis-inducing therapies. Conventional chemotherapeutics are known to induce apoptosis but do so nonspecifically by targeting multiple cellular processes, which can lead to both therapy resistance and a narrowing of the therapeutic window. Promoting apoptosis as a strategy for cancer drug discovery enables therapeutic agents to selectively induce apoptosis in cancer cells while improving therapeutic outcomes (*33–36*). In such a scenario, PET apoptosis imaging can be used to monitor the effect of apoptosis-inducing or -promoting drug treatments with the aim of predicting responders to such therapies perhaps earlier than metabolic ^{18}F-FDG PET imaging. For such a strategy to be successful, the PET

TABLE 3
Organ Doses for ^{18}F-CP-18 and ^{18}F-FDG for 4.8-H Bladder-Voiding Interval

Organ	^{18}F-CP-18 (μGy/MBq)	^{18}F-FDG (μGy/MBq)
Adrenals	6.8	13
Brain	2.4	19
Breasts	7.7	9.2
Gallbladder wall	7.6	14
Lower large intestine wall	20	17
Small intestine	11	14
Stomach wall	6.1	13
Upper large intestine wall	10	13
Heart wall	10	60
Kidneys	39	20
Liver	11	16
Lungs	4.7	17
Muscle	8.1	11
Ovaries	19	17
Pancreas	6.9	26
Red marrow	6.8	13
Osteogenic cells	7.9	12
Skin	4.7	8.4
Spleen	13	37
Testes	25	13
Thymus	4.8	12
Thyroid	4.2	10
Urinary bladder wall	540	190
Uterus	38	23

imaging data must be correlated with clinical, surgical, pathologic, and patient outcomes. PET imaging of caspase-3 could therefore be established as a pharmacodynamic biomarker to measure the increase in apoptotic fraction after treatment, allowing clinicians to tailor patient treatments or optimize dosing regimens. Further studies are needed to evaluate the efficacy of this promising PET imaging agent.

CONCLUSION

The injection of ^{18}F-CP-18 did not cause clinically significant changes in vital signs or blood tests, suggesting that the administration of ^{18}F-CP-18 is both safe from a dosimetry perspective and compatible with PET imaging in humans.

DISCLOSURE

The costs of publication of this article were defrayed in part by the payment of page charges. Therefore, and solely to indicate this fact, this article is hereby marked "advertisement" in accordance with 18 USC section 1734. The study was supported by Siemens Molecular Imaging Inc. The study was conducted at Fox Chase Cancer Center under the ClinicalTrials.gov Identifier NCT01362712. No other potential conflict of interest relevant to this article was reported.

ACKNOWLEDGMENTS

We thank Donna Mosley and Nuclear Medicine staff for their help with patient data acquisition. We thank Mary Benetz and the staff from the Protocol Management Office, Clinical Research Unit and Protocol Support Laboratory, for their help with the research protocol.

REFERENCES

1. Elmore S. Apoptosis: a review of programmed cell death. *Toxicol Pathol.* 2007;35:495–516.
2. Graeber TG, Osmanian C, Jacks T, et al. Hypoxia-mediated selection of cells with diminished apoptotic potential in solid tumours. *Nature.* 1996;379:88–91.
3. Kunz M, Ibrahim SM. Molecular responses to hypoxia in tumor cells. *Mol Cancer.* 2003;2:23.
4. Reshef A, Shirvan A, Waterhouse RN, et al. Molecular imaging of neurovascular cell death in experimental cerebral stroke by PET. *J Nucl Med.* 2008;49:1520–1528.
5. Cohen A, Shirvan A, Levin G, Grimberg H, Reshef A, Ziv I. From the Gla domain to a novel small-molecule detector of apoptosis. *Cell Res.* 2009;19:625–637.
6. Höglund J, Shirvan A, Antoni G, et al. ^{18}F-ML-10, a PET tracer for apoptosis: first human study. *J Nucl Med.* 2011;52:720–725.
7. Wang F, Fang W, Zhang MR, et al. Evaluation of chemotherapy response in VX2 rabbit lung cancer with ^{18}F-labeled C2A domain of synaptotagmin I. *J Nucl Med.* 2011;52:592–599.
8. Grierson JR, Yagle KJ, Eary JF, et al. Production of [F-18]fluoroannexin for imaging apoptosis with PET. *Bioconjug Chem.* 2004;15:373–379.
9. Toretsky J, Levenson A, Weinberg IN, Tait JF, Uren A, Mease RC. Preparation of F-18 labeled annexin V: a potential PET radiopharmaceutical for imaging cell death. *Nucl Med Biol.* 2004;31:747–752.
10. Yagle KJ, Eary JF, Tait JF, et al. Evaluation of ^{18}F-annexin V as a PET imaging agent in an animal model of apoptosis. *J Nucl Med.* 2005;46:658–666.
11. Madar I, Ravert H, Nelkin B, et al. Characterization of membrane potential-dependent uptake of the novel PET tracer ^{18}F-fluorobenzyl triphenylphosphonium cation. *Eur J Nucl Med Mol Imaging.* 2007;34:2057–2065.
12. Madar I, Huang Y, Ravert H, et al. Detection and quantification of the evolution dynamics of apoptosis using the PET voltage sensor ^{18}F-fluorobenzyl triphenyl phosphonium. *J Nucl Med.* 2009;50:774–780.
13. Reshef A, Shirvan A, Akselrod-Ballin A, Wall A, Ziv I. Small-molecule biomarkers for clinical PET imaging of apoptosis. *J Nucl Med.* 2010;51:837–840.
14. Faust A, Wagner S, Law MP, et al. The nonpeptidyl caspase binding radioligand (S)-1-(4-(2-[^{18}F]Fluoroethoxy)-benzyl)-5-[1-(2-methoxymethylpyrrolidinyl)sulfonyl] isatin ([^{18}F]CbR) as potential positron emission tomography-compatible apoptosis imaging agent. *Q J Nucl Med Mol Imaging.* 2007;51:67–73.
15. Smith G, Glaser M, Perumal M, et al. Design, synthesis, and biological characterization of a caspase 3/7 selective isatin labeled with 2-[^{18}F]fluoroethylazide. *J Med Chem.* 2008;51:8057–8067.
16. Nguyen QD, Smith G, Glaser M, Perumal M, Arstad E, Aboagye EO. Positron emission tomography imaging of drug-induced tumor apoptosis with a caspase-3/7 specific [^{18}F]-labeled isatin sulfonamide. *Proc Natl Acad Sci USA.* 2009; 106:16375–16380.
17. Podichetty AK, Faust A, Kopka K, et al. Fluorinated isatin derivatives. Part 1: synthesis of new N-substituted (S)-5-[1-(2-methoxymethylpyrrolidinyl)sulfonyl] isatins as potent caspase-3 and -7 inhibitors. *Bioorg Med Chem.* 2009;17:2680–2688.
18. Podichetty AK, Wagner S, Schroer S, et al. Fluorinated isatin derivatives. Part 2. New N-substituted 5-pyrrolidinylsulfonyl isatins as potential tools for molecular imaging of caspases in apoptosis. *J Med Chem.* 2009;52:3484–3495.
19. Zhou D, Chu W, Chen D, et al. [^{18}F]- and [^{11}C]-labelled N-benzyl-isatin sulfonamide analogues as PET tracers for apoptosis: synthesis, radiolabeling mechanism, and in vivo imaging of apoptosis in Fas-treated mice using [^{11}C]WC-98. *Org Biomol Chem.* 2009;7:1337–1348.
20. Nguyen QD, Challapalli A, Smith G, Fortt R, Aboagye EO. Imaging apoptosis with positron emission tomography: 'bench to bedside' development of the caspase-3/7 specific radiotracer [^{18}F]ICMT-11. *Eur J Cancer.* 2012;48:432–440.
21. Zhou D, Chu W, Rothfuss J, et al. Synthesis, radiolabeling, and in vivo evaluation of an ^{18}F-labeled isatin analog for imaging caspase-3 activation in apoptosis. *Bioorg Med Chem Lett.* 2006;16:5041–5046.
22. Niu G, Chen X. Apoptosis imaging: beyond annexin V. *J Nucl Med.* 2010;51: 1659–1662.
23. Talanian RV, Quinlan C, Trautz S, et al. Substrate specificities of caspase family proteases. *J Biol Chem.* 1997;272:9677–9682.
24. Walsh JC, Kolb HC. Applications of click chemistry in radiopharmaceutical development. *Chimia (Aarau).* 2010;64:29–33.
25. Marik J, Sutcliffe JL. Click for PET: rapid preparation of [^{18}F]fluoropeptides using CuI catalyzed 1,3-dipolar cycloaddition. *Tetrahedron Lett.* 2006;47:6681–6684.
26. Mamat C, Ramenda T, Wuest FR. Recent applications of click chemistry for the synthesis of radiotracers for molecular imaging. *Mini Rev Org Chem.* 2009;6:21–34.
27. Su H, Chen G, Gangadharmath U, et al. Evaluation of [^{18}F]-CP18 as a PET imaging tracer for apoptosis. *Mol Imaging Biol.* May 17, 2013 [Epub ahead of print].
28. Stabin MG, Sparks RB, Crowe E. OLINDA/EXM: the second-generation personal computer software for internal dose assessment in nuclear medicine. *J Nucl Med.* 2005;46:1023–1027.
29. Food and Drug Administration. Guidance for Industry and Researchers. The Radioactive Drug Research Committee: Human Research Without An Investigational New Drug Application. August 2010. Available at: http://www.fda.gov/downloads/Drugs/GuidanceComplianceRegulatoryInformation/Guidances/UCM163892.pdf. Accessed September 24, 2013.
30. Stabin M, Stubbs J, Toohey R. *Radiation Dose Estimates for Radiopharmaceuticals, NUREG/CR-6345.* April 1996. Available at: http://www.nrc.gov/reading-rm/doc-collections/nuregs/contract/cr6345/cr6345.pdf. Accessed September 24, 2013.
31. Krajewska M, Wang HG, Krajewski S, et al. Immunohistochemical analysis of in vivo patterns of expression of CPP32 (caspase-3), a cell death protease. *Cancer Res.* 1997;57:1605–1613.
32. Kurihara H, Yang DJ, Cristofanilli M, et al. Imaging and dosimetry of ^{99m}Tc EC annexin V: preliminary clinical study targeting apoptosis in breast tumors. *Appl Radiat Isot.* 2008;66:1175–1182.
33. Fischer U, Schulze-Osthoff K. Apoptosis-based therapies and drug targets. *Cell Death Differ.* 2005;12(suppl 1):942–961.
34. Gillies RJ, Verduzco D, Gatenby RA. Evolutionary dynamics of carcinogenesis and why targeted therapy does not work. *Nat Rev Cancer.* 2012;12:487–493.
35. Jendrossek V. The intrinsic apoptosis pathways as a target in anticancer therapy. *Curr Pharm Biotechnol.* 2012;13:1426–1438.
36. Sayers TJ. Targeting the extrinsic apoptosis signaling pathway for cancer therapy. *Cancer Immunol Immunother.* 2011;60:1173–1180.